Characterization of Magnetic Nanoparticle-Seeded Microspheres for Magnetomotive and Multimodal Imaging

Marina Marjanovic, Freddy T. Nguyen, Adeel Ahmad, Pin-Chieh Huang, Kenneth S. Suslick, and Stephen A. Boppart, *Fellow, IEEE*

***Abstract*—Magnetic iron-oxide nanoparticles have been developed as contrast agents in magnetic resonance imaging (MRI) and as therapeutic agents in magnetic hyperthermia. They have also recently been demonstrated as contrast and elastography agents in magnetomotive optical coherence tomography (MM-OCT) and elastography. Protein-shell microspheres containing suspensions of these magnetic nanoparticles in lipid cores, and with functionalized outer shells for specific targeting, have also been demonstrated as efficient contrast agents for imaging modalities such as MM-OCT and MRI, and can be easily modified for other modalities such as ultrasound, fluorescence, and luminescence imaging. By leveraging the benefits of these various imaging modalities with the use of only a single agent, a magnetic microsphere, it becomes possible to use a wide-field imaging method (such as MRI or small animal fluorescence imaging) to initially locate the agent, and then use MM-OCT to obtain dynamic contrast images with cellular level morphological resolution. In addition to multimodal contrast-enhanced imaging, these microspheres could serve as drug carriers for targeted delivery under image guidance. Although the preparation and surface modifications of protein microspheres containing iron oxide nanoparticles have been previously described and feasibility studies conducted, many questions regarding their production and properties remain. Since the use of multifunctional microspheres could have high clinical relevance, here we report a detailed characterization of their properties and behavior in different environments to highlight their versatility. The work presented here is an effort for the development and optimization of nanoparticle-based microspheres as multimodal contrast agents that can bridge imaging modalities on different size scales, especially for their use in MM-OCT and MRI.**

Manuscript received April 13, 2018; revised June 19, 2018 and July 5, 2018; accepted July 9, 2018. Date of publication July 16, 2018; date of current version August 6, 2018. This work was supported by the National Institutes of Health under Grants R01 CA166309 and R01 CA213149. *(Corresponding author: Stephen A. Boppart.)*

M. Marjanovic and P.-C. Huang are with the Department of Bioengineering, University of Illinois at Urbana-Champaign, Urbana, IL 61801 USA (e-mail: marinam@illinois.edu; phuang16@illinois.edu).

F. T. Nguyen was with the University of Illinois at Urbana-Champaign, Urbana, IL 61801 USA. He is now with the Massachusetts Institute of Technology, Cambridge, MA 02139 USA (e-mail: freddytn@mit.edu).

A. Ahmad was with the University of Illinois at Urbana-Champaign, Urbana, IL 61801 USA. He is now with Texas Instruments, Dallas, TX 75243 USA (e-mail: aahmad5@ti.com).

K. S. Suslick is with the Department of Chemistry, University of Illinois at Urbana-Champaign, Urbana, IL 61801 USA (e-mail: ksuslick@illinois.edu).

S. A. Boppart is with the Department of Electrical and Computer Engineering and Bioengineering, Beckman Institute for Advanced Science and Technology, University of Illinois at Urbana-Champaign, Urbana, IL 61801 USA (e-mail: boppart@illinois.edu).

Color versions of one or more of the figures in this paper are available online at http://ieeexplore.ieee.org.

Digital Object Identifier 10.1109/JSTQE.2018.2856582

***Index Terms*—Contrast agents, multimodal imaging, protein microspheres, targeted drug delivery.**

I. Introduction

THE trend in biomedical imaging for developing agents for early detection and diagnosis of disease is rapidly expanding toward their concomitant use for treatment. Since virtually all diseases originate at the molecular and cellular level, detection and imaging systems with resolutions and sensitivities capable of imaging at these levels, in addition to the systemic level (such as MRI and ultrasound imaging) would be most suitable. As such, optical imaging has played a central role, providing not only sufficient resolution to resolve morphological features at the cellular level, but also wavelength sensitivity which enables the detection and localization of the optical signal from spectroscopically-specific endogenous molecules or exogenous molecules or agents. The mere presence of spectroscopically-identifiable agents, however, has limited informational content unless the presence can be linked to some physiologically- or functionally-meaningful parameter. By functionalizing and targeting agents to specific cells and molecular sites, the detection and spatial localization of the agents through imaging techniques adds molecular specificity. The potential for molecular imaging therefore becomes broad, providing morphological, spatial, and functional information at the molecular level.

Most of the optical probes developed in recent years have been based on the emission of a bioluminescent or fluorescent signal. While these methods now have an established track record of use, there remains a number of other optical imaging methods that would equally benefit from novel optical agents that could not only non-specifically enhance contrast within images, but ultimately provide the same molecular specificity as the bioluminescent and fluorescent probes. Optical Coherence Tomography (OCT) is an optical technique that is analogous to ultrasound imaging, but instead of using sound waves, OCT uses low-coherence (broadband) light, enabling high-resolution, non-invasive, imaging of microscopic structures. One limitation of OCT is the shallow depth of imaging (up to $\sim$2 mm) in highly scattering tissues, which primarily depends on the optical scattering and absorption properties of different tissues [1], [2]. In recent years, much effort has been put into developing molecularly-targeted contrast agents which enhance the

imaging capabilities of OCT. These include scattering microspheres as contrast and drug-delivery agents, magnetomotive nanoparticles, plasmon-resonant nanoparticles, and absorbing near-infrared dyes. In addition, there is a large number of optical properties and characteristics of contrast agents that can be leveraged to enable molecular imaging of cells and tissues. Strategies to generate molecular contrast in images have evolved dramatically in the past two decades from traditional dyes to highly sophisticated molecular agents that are generally sized in the range of hundreds of microns down to a few nanometers [3]–[5].

Magnetomotive optical coherence tomography (MM-OCT) is a novel extension of OCT for imaging a distribution of magnetic molecular imaging agents in biological specimens [6]. Magnetomotion of contrast agents through an externally-modulating magnetic field is an excellent mechanism for achieving dynamic contrast. Human tissue exhibits an extremely weak magnetic susceptibility ($\chi < 10^{-5}$). To obtain good magnetic contrast, magnetic probes, such as superparamagnetic iron oxide nanoparticles with $\chi = \sim 1$, can be used. In the presence of a magnetic field gradient, magnetic nanoparticles (MNPs) with high magnetic susceptibility experience a gradient force, and rotate to align their internal magnetization along the field. If they are embedded in tissue, the resulting magnetomotion of the MNPs and the perturbation of the surrounding cells and extracellular matrix result in a change in the optical scattering properties of the local tissue microenvironment. In an elastic medium, the particles return to their original position and orientation after removal of the magnetic field. This permits modulation of their position by repetitively modulating the magnetic field. The resulting increase in contrast due to magnetomotion can be effectively detected by an OCT system.

The interaction between the MNPs and the surrounding microenvironment also allows measurement of biomechanical properties at the tissue, cellular, and even the molecular level. Magnetomotion is induced through the interaction of an external magnetic field with MNPs distributed in the tissues and cells [6], [7]. The displacement depends on the viscoelastic properties of the microenvironment and can be measured with nanometer-scale sensitivity using magnetomotive optical coherence elastography (MM-OCE). This latest OCT technique combines the advantages of localized magnetomotive contrast with fast real-time non-invasive optical imaging to quantify the dynamic micromechanical properties of viscoelastic materials [8].

In MM-OCT and MM-OCE, dynamic contrast is generated by utilizing the nanoscale displacements of magnetic nano- or micro-particles induced by an external magnetic field. While a single MNP would not necessarily induce a measurable displacement of bound cell and tissue structures due to its small size, a minimum concentration of magnetic particles within a resolution volume of the OCT system is required to measure a detectable magnetomotive signal [9], as the combined effect of closely spaced MNPs will induce larger tissue displacements. The minimum concentration of MNPs needed depends on the magnetic field characteristics of the coil, the magnetic properties of the MNPs, and the mechanical and magnetic properties of the surrounding MNP-laden area. The magnetomotive force on the magnetic particles can be increased by increasing the size of the particles or packing together a number of MNPs inside larger sized carriers, such as microspheres.

Protein-shell microspheres filled with suspensions of iron oxide nanoparticles and fluorescent dye in oil can be used as multimodal contrast agents in MM-OCT, fluorescence imaging, ultrasound imaging, and magnetic resonance imaging (MRI) [10], [11]. These microspheres are made using a sonication process, which allows the proteins to form a shell encapsulating the oil and hydrophobic iron oxide nanoparticles [12]. Traditionally, similar microspheres have been filled with perfluorocarbon and used for ultrasound imaging. However, the introduction of oil in the inner core has resulted in a much more stable and longer lasting contrast agent, extending its lifetime from days to several months. Just like MNPs, microspheres containing iron oxide nanoparticles in their core can be modulated externally using a magnetic field to create dynamic MM-OCT contrast. In addition, these microspheres can be readily functionalized for specific binding to biomarkers that are overexpressed in tumors [10]–[12] or atherosclerotic lesions [13]. They are also receiving attention in other biological and biomedical applications such as drug delivery, enzyme immobilization, cell isolation, protein purification and DNA separation [11].

Surface-functionalized microspheres encapsulated with hydrophobic drugs such as paclitaxel could provide a molecularly-targeted method for killing single tumor cells [14]. For example, microspheres specifically bound to tumor cells could be externally controlled by an alternating magnetic field or ultrasound waves to trigger their rupture or the controlled release of their contents into the local vasculature or the local extracellular matrix of the targeted area [4].

Together, MM-OCT and MM-OCE offer a unique dynamic methodology in biomedical imaging and sensing for providing targeted contrast enhancement and/or sampling of the local biomechanical properties of the microenvironment. Both fundamental physical discoveries and new biological and medical applications are likely to continue to emerge using these techniques. Recent *in vitro* and *in vivo* studies confirmed the biocompatibility of the microspheres and the extracts of the microspheres showed no cytotoxic reactivity in the cytotoxicity tests [15], [16]. Experiments also showed that polylactic acid (PLA) coated microspheres containing superparamagnetic Fe_3O_4 nanoparticles, injected in mice, had no effect on their main organs and blood biochemistry, its performance conforms to clinical requirements, and its biocompatibility conforms to the standard for medical materials [16].

This study reported here follows the research of Suslick and co-workers who have developed the sonochemical method to prepare aqueous solution of protein microcapsules filled with water-insoluble fluids [17]–[19]. Although the application of iron oxide MNP-filled protein microspheres has been described in a number of cases, to explore the feasibility of their use in translational studies, there is a need to optimize their fabrication to maximize their MM-OCT signal and understand how it relates to the MRI signal. Here we aim to provide a detailed specification of these microspheres using MM-OCT and MRI, including their scattering and magnetic properties, their evaluation in different media, and their potential as a cancer biomarker both *in vitro* and *in vivo*.

II. Materials and Methods

A. Microsphere Preparation and Shell Modifications

Iron oxide nanoparticle (Sigma Aldrich, 544884-25G) encapsulated microspheres were prepared using a sonication method described previously [10]. The same layer-by-layer (LBL) adhesion method was used to modify the protein shell and for some experiments, microspheres were functionalized with an arginine-glycine-aspartic acid (RGD) peptide sequence. Microspheres were kept in the refrigerator with continuous rotation to prevent settling and aggregation. The size of the microspheres was determined using dynamic light scattering (DLS) measurements (Accusizer FX Particle Sizer), and their morphology was assessed using transmission electron microscope (TEM) and scanning electron microscope (SEM).

Prepared microspheres were washed with PBS (pH 7.4) 5–10 times, and approximately 15×10^6 microspheres were re-suspended in 850 μL of PBS and 500 μL of 14% gluteraldehyde solution. The suspension was vortexed and then fixed at room temperature for two hours on the rotating rotisserie shaker. After the incubation period, the microspheres were washed three times in a 0.1 M Na-cacodylate buffer (pH 7.4) and the microsphere layer was isolated by centrifugation at 6000 RPM for 5 minutes. The microspheres were stained for two hours with 1% osmium tetroxide in a 0.1 M Na-cacodylate buffer (pH 7.4) solution on the rotisserie shaker and then again washed three times in only 0.1 M Na-cacodylate buffer (pH 7.4). The microspheres were gradually dehydrated by incubation in ethanol solutions with progressively increased concentration (10, 25, 50, 75, 95, and 100% ethanol) for five minutes in each solution. After two more washes with 100% hexamethyldislazane (HMDS), microspheres were re-suspended in HMDS and allowed to air dry on nitrocellulose membrane filters (0.22 μm pore size, 13 mm diameter) under a chemical fume hood. This method of depositing and drying the microspheres proved to be much more efficient than critical point drying. The latter process often resulted in a filmy layer from the dried alcohol or other solvents on top of the microspheres, hindering the ability to visualize the finer structures on their surface. Samples were made conductive for SEM imaging by sputter coating for 90 seconds to achieve a $\sim$20 nm layer of gold/palladium coating using a turbo-pumped sputter coater (Denton Vacuum – Model # Desk-1 TSC). The thicker coating permitted the use of higher beam intensity and longer imaging times which enabled higher resolution and sharper images. If the coating was too thin, the microspheres easily shriveled and collapsed under the high-power beam intensities or under long acquisition time periods of the electron beam. Samples were imaged using a SEM (FEI Company – Phillips 30 ESEM-FEG) with an electron beam intensity of 5.0 kV, a working distance of 3.2 mm, and magnifications ranging from 6,000X to 120,000X.

The processing of microspheres for TEM followed the same procedure for the fixation, washing, staining, and dehydration steps. However, after the last dehydration step when the microspheres were re-suspended in 100% ethanol, the fixed microspheres were washed and infiltrated with an epoxy resin. The microspheres were first re-suspended in a 1:1 mixture of acetonitrile and the EMbed-812 with DMP-30 epoxy resin solution for ten minutes, and then in 100% epoxy resin solution overnight at room temperature. The embedded samples were cured in a vacuum sealed oven at 60 °C for a minimum of three days and then sectioned using a diamond knife in 100 nm slices on an ultramicrotome (Leica Ultracut UCT). The sections were placed on copper mesh grids (Electron Microscopy Sciences, 200 Mesh Copper Gilder Grids, G200-Cu) and imaged using a TEM (Philips CM200) at a voltage of 120 kV.

B. Iron-Oxide Nanoparticle-Based Microspheres as a Contrast Agent for MM-OCT and MRI

The scattering properties of nanoparticle-based microspheres and their displacement in a magnetic field were performed with 1.0×10^7 microspheres in each sample. MM-OCT imaging of samples was performed with a spectral-domain OCT system using a Ti:Al_2O_3 femtosecond laser (KMLabs, Inc.) as a light source, which was described previously [9]. The light, with a bandwidth of 120 nm centered at 800 nm, provided $\sim$3 μm axial imaging resolution. A magnetic field of $\sim$0.08 T and a gradient of $\sim$15 T/m was produced within the sample imaging volume using a water-cooled magnet. The light beam on the sample was scanned through the central bore of the solenoid and the interference between the reference and sample beams was measured with a custom-made spectrometer, providing 2 mm imaging depth. MM-OCT imaging was done at 100 Hz and 200 Hz, with a scan rate of 1000 A-scans/sec.

A 14.1 T Varian system with an 89 mm bore size and 600 MHz Varian Unity/Inova NMR spectrometer was used for MRI measurements. Measurements were taken at four different echo times of 3.3 ms, 5.0 ms, 7.0 ms, and 9.0 ms, and nineteen MRI slices were taken throughout the full volume of the gel in the capillary tubes to create a standard curve and calculate the relaxation times ($T2^*$) using a Matlab script.

C. In Vitro *Targeting of Cancer Cells*

For a flow cytometry study of $\alpha_v\beta_3$ integrin receptor expression on various cancer cell lines, confluent monolayers of cells were cultured in Petri dishes. The cells were washed with warm (37 °C) sterile PBS three times to ensure the complete removal of cell culture medium. The cells were trypsinized with 1X trypsin (0.05% trypsin, 0.2 g/L EDTA, 0.85 g/L NaCl). After 10–15 minutes, the cells detached from the bottom of the cell culture dishes and were re-suspended in their respective culture medium to rapidly deactivate the trypsin. Cells were subsequently centrifuged at 1500 rpm for 5 minutes and washed once more to remove any residual trypsin. The cells were then re-suspended in sterile PBS and counted using a hemocytometer. Four aliquots of 1×10^6 cells (one negative staining control and three positive controls) for each cell line were prepared in cold buffer solution (1X PBS, 1% BSA, 0.5 mm EDTA) and the primary $\alpha_v\beta_3$ integrin antibody (mouse monoclonal IgG1, GeneTex cat. #GTX4013) was added to each of three cell aliquots marked for positive staining at a concentration of 1 μg per 1×10^6 cells. This step labels exposed $\alpha_v\beta_3$ integrin

receptors on the cell surface. The cells were then incubated at 4 °C on an orbital shaker set at ∼200 rpm for 30 minutes.

After washing cells twice with cold buffer solution, the secondary antibody (anti-mouse conjugated with FITC) was added to all four aliquots of cells at a concentration of 1 μg per 1×10^6 cells. The samples were covered with foil and placed on an orbital shaker at ∼200 rpm and incubated at 4 °C for 30 minutes. The cells were washed twice with cold buffer solution and then re-suspended in 300 μL of the cold PBS. The cells were maintained on ice and covered with foil until they could be analyzed by flow cytometry.

The flow cytometry was performed with a BD Biosciences LSR II system. The first step involved taking measurements of a FITC fluorescent bead standards (Bang Laboratories, #555A, Quantum FITC-5 MESF). There were five different standards in this particular kit of five populations of 7–9 μm beads, each with different levels of FITC fluorescence intensities per bead. Comparison of stained samples to the standards allowed quantification of fluorescent particles per scattering particle (the cell) through the flow channel.

Ten thousand optical scattering events (or cells) were collected for each aliquot (triplicate positive staining controls and one negative control). The data were analyzed using FCS Express software (DeNovo Software). Each data set was initially gated in a plot of the forward optical scattering against the side optical scattering signal in order to exclude non-cellular particles. A second gating was made to isolate live cells versus dead cells by plotting the forward optical scattering width against the forward optical scattering amplitude. The resulting FITC intensity fluorescence peak was identified using the median channel value. These channel values were converted to MESF/ABC values using the standard curve previously established. The MESF/ABC corresponds to the measured fluorescence intensity per cell. The MESF/ABC values for the positively stained cells were subtracted by the MESF/ABC values of the negative controls. The resulting values were averaged across triplicate samples for each cell line and reported as the ratio of specific binding (positively stained minus negatively stained) to non-specific binding (negatively stained) for easier comparison of the expression results from flow cytometry to the fluorescence microscopy of the targeting data *in vitro*.

For fluorescence imaging experiments, microspheres with encapsulated iron oxide nanoparticles and Nile Red dye were used to assess the targeting of the microspheres to $\alpha_v\beta_3$ integrin receptors expressed on various cell lines. Using the LBL adhesion method, microspheres were coated with a layer of PDDA followed by a layer of silica. One batch of microspheres was additionally coated with a layer of RGD, and a second batch of microspheres remained uncoated at the silica layer. Cancer cell lines were chosen to provide a spectrum of $\alpha_v\beta_3$ receptor expression levels and approximately 100,000 cells from each cancer cell line (Table I) were seeded into each well of a 4-well chamber slide. The seeding density of the cell cultures used was about 50% confluence to allow the cells to form a uniform monolayer of cells within 24 hours.

The cells were then washed three times with sterile PBS to remove any floating or dead cells. For each cell line, two of the four wells were incubated with RGD-functionalized microspheres and the other two wells were incubated with non-functionalized microspheres. Each well in the chamber slide was incubated with $\sim 4 \times 10^5$ of microspheres for 1 hr. After the incubation, cells were washed twice with sterile PBS to remove any unbound microspheres and re-suspended in culture medium until the time of imaging. During fluorescence imaging, the cell medium was removed and PBS was added to reduce background fluorescence coming from the cell medium. Multidimensional acquisition of both fluorescence and brightfield images was taken using a 20X objective on a Zeiss Axiovert 200 inverted microscope. Images were acquired at ten different locations with similar densities of cells for each sample. Images in the fluorescence channel were taken using the auto-exposure setting to take advantage of the full dynamic range of the detection system and to reduce the chances of saturating the camera. The percent increase in fluorescence was calculated by comparing average fluorescence intensities of RGD-functionalized vs. non-functionalized microspheres bound to each cell line, to give the ratio of specific binding of the RGD-functionalized microspheres to the non-specific binding of the non-functionalized microspheres to the $\alpha_v\beta_3$ integrin receptors.

TABLE I
CANCER CELL LINES WITH DIFFERENT LEVELS OF $\alpha_v\beta_3$ INTEGRIN EXPRESSION, USED FOR THE EVALUATION OF THE BINDING SPECIFICITY AND AFFINITY OF THE MICROSPHERES FOR THE INTEGRIN RECEPTOR

Cell Line	ATCC #	Description
HT-29	HTB-38	Human colorectal adenocarcinoma
SK-BR-3	HTB-30	Human breast adenocarcinoma
MCF-7	HTB-22	Human breast adenocarcinoma
hTERT-HME1	CRL-4010	Human breast immortalized
ZR-75-1	CRL-1500	Human breast ductal carcinoma
MDA-MB-231	HTB-26	Human breast adenocarcinoma
MDA-MB-435S	HTB-129	Human breast ductal carcinoma

D. MM-OCT Imaging in Different Biological Environments

Animal tumor models were used to demonstrate the feasibility of the nanoparticle-based protein microspheres as a contrast agent in biological environments. The N-methyl-N-nitrosourea (NMU) carcinogen-induced rat mammary tumor model produces mammary tumors 8–10 weeks after injection.

All experiments were performed in compliance with an experimental protocol approved by the Institutional Animal Care and Use Committee at the University of Illinois at Urbana-Champaign. Wistar–Furth female inbred rats (32 days old) (Jackson Labs, Bar Harbor, ME, USA) were used in this study. The rats were individually housed, fed standard rat chow pellets, and provided with water and food ad libitum.

NMU (50 mg/kg body weight) was injected intraperitoneally (i.p.) twice, at a 1-week interval. The first injection was made in the left side and the second injection in the right side of the peritoneum. Following NMU injections, animals were palpated weekly to assess mammary tumor development. For tumor

sampling, rats were euthanized by CO_2 inhalation and excised tumors were injected with microspheres for MM-OCT imaging.

E. In Vivo *Targeting in a Pre-Clinical Cancer Model*

The same rat mammary tumor model was used for *in vivo* targeting experiments. Microsphere suspensions (1 mL; $\sim 10^9$ microspheres) were injected into the jugular vein of an anesthetized rat, which corresponded to 0.17–0.22 mmol of iron oxide/kg body weight. The injected dose of iron oxide corresponds to clinically approved doses of gadolinium-based contrast agents (GBCAs) [20] and carbohydrate-coated, superparamagnetic iron oxide nanoparticles [21]. Imaging was performed immediately after the rat was euthanized by CO_2 inhalation. Abdominal skin and muscles were first resected, and exposed tumors and other organs were imaged while still inside the surgical cavity. Whole-body and isolated organ fluorescence imaging were performed on a Maestro Imaging System (CRi, Inc.; Woburn, MA, excitation 575–605 nm, emission 655 nm longpass). Tumors were subsequently excised for fluorescence and MM-OCT imaging.

III. Results and Discussion

A. Microsphere Preparation and Shell Modifications

There are three main steps in the sonochemical synthesis of these protein-shell oil-core microspheres: 1) emulsification, 2) protein aggregation at the oil/water interface, and 3) chemical crosslinking of proteins in the shell. The preparation protocol of these microspheres has been described previously in several publications [10], [12]. A 70/30 mixture of bovine serum albumin (BSA) protein and vegetable oil solution, already containing iron oxide nanoparticles (Fe_3O_4) and Nile Red fluorescence dye, was sonicated by using a high intensity ultrasound horn at a frequency of 20 kHz, at an acoustic power of 35 W/cm^2 ($T = 45^{\circ}C$). The surfactant used to emulsify the microspheres is one of the main controlling factors in the size determination of the protein microspheres since it affects the surface tension between the oil and protein. The fluorescent dye was used as a spectral tag to identify microsphere binding in targeting experiments, but could also be used for fluorescence-based imaging applications. The size of these microspheres can be fabricated in the range from 200 nm to 10 μm in diameter, depending on the frequency and power of the ultrasound sonication, but most of the microspheres were in the 1–3 μm range at these sonication parameters. A dynamic light scattering (DLS) instrument (Accusizer FX Particle Sizer) was used to measure the size distribution and the concentration of microspheres. For size separation, a standard filtration method was used.

The structure of these protein microspheres is composed of three main compartments: the inner hydrophobic core, the outer hydrophilic protein shell, and the surface of the shell, highly charged due to the numerous ionized groups present on the BSA molecules. Each of these components can incorporate a varying number of nanoparticles, dyes, and ligands to provide contrast or add functionality to the protein microspheres. For this study, a previously described electrostatic adhesion approach was used for the surface modification by a layer-by-layer (LBL) self-assembly process, where macromolecules are used for the deposition of material one layer at a time to the template surface. As one example, the microsphere surface was functionalized by adding layers of polydimethyl diallyl chloride (PDDA), followed by silica nanoparticles ($\sim$100 nm). The PDDA layer reversed the charge of the surface and thereby enabled the coating of silica nanoparticles. An RGD peptide sequence attached to a poly-lysine sequence (linear sequence of amino acids, RGDKKKKKK) was layered on top of the silica. Since RGD is not highly positively charged, a poly-lysine sequence facilitates the adhesion of RGD on the surface of microspheres. Although this approach can be used with variety of ligands, its effectiveness is demonstrated with the small tripeptide RGD to selectively target $\alpha_v\beta_3$ integrin receptors. It has been shown that integrin receptors are over-expressed in cancer cells and tumor vasculature [22], [23] and atherosclerotic vascular diseases [24], [25]. There are over 25 known integrin receptors and most of these receptors 'recognize' the small tri-peptide sequence RGD [24].

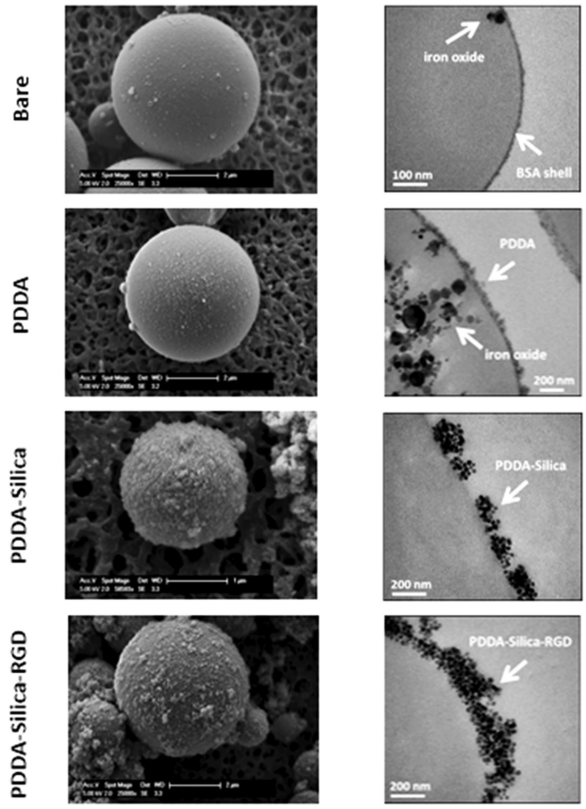

Fig. 1. Representative SEM (left) and TEM (right) images of protein microspheres after each layering process. From top down: bare microspheres before any layering; PDDA layered directly onto the bare microspheres; bare microspheres layered with PDDA and silica; bare microspheres layered with PDDA followed by silica and RGD. Iron oxide particles can be seen in the oil core of the microspheres.

Scanning electron microscope (SEM) images of bare microspheres, PDDA-coated microspheres, PDDA-silica coated microspheres, and PDDA-silica-RGD coated microspheres are shown in Fig. 1. The microspheres were 1–5 μm in size, which was in agreement with the results from the DLS measurements.

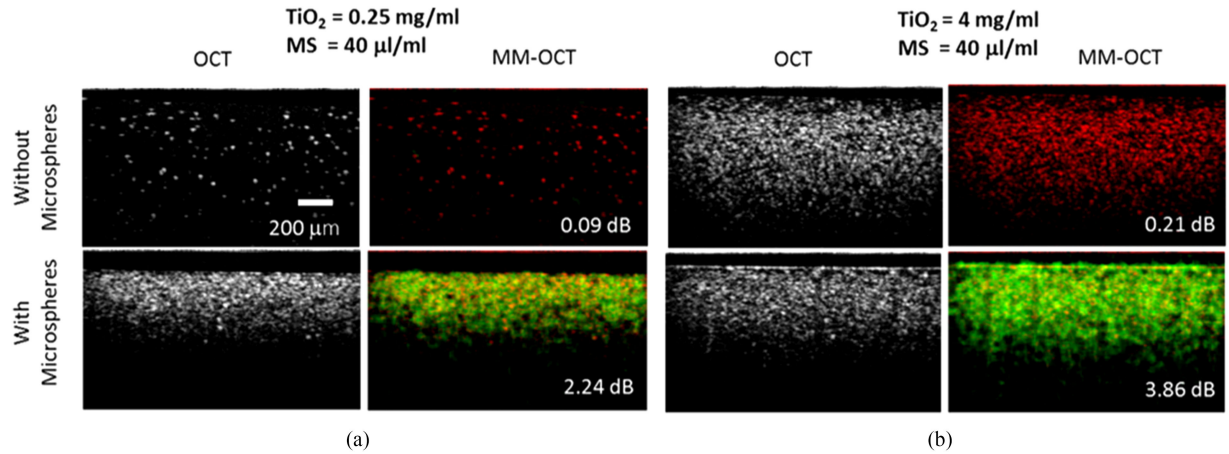

Fig. 2. Contrast enhancement with MNP-seeded microspheres. OCT structural and MM-OCT images of agarose phantoms with and without the addition of microspheres. (a) Low background optical scattering, and (b) high background optical scattering, using different concentrations of TiO_2. The red color channel represents the intensity level of structural OCT, while the green channel represents the level of magnetomotive signal. The signal from high optical scattering environments is enhanced by the magentomotive signal (green channel) coming from the MNP-seeded microspheres. The decibel (dB) values represent the magnetomotive signal strength in a relative manner. The extraction of MM-OCT signal involved normalizing the modulated vibrational signal acquired with the magnetic field turned on ("field-on") over that acquired with the magnetic field turned off ("field off"). Scale bar applies to all images.

Differences in the nanoscale texture of the surface of the microspheres can be visualized with each added layer. Aggregates of protein microspheres were found in small numbers and were not a major issue for most of the coatings except for the PDDA coated microspheres. Microspheres coated with silica settled in solution under gravity, making them more suitable for *in vitro* studies where the cells are attached to the bottom of the culture dish.

TEM images of each layer show the presence of iron oxide nanoparticles in the microspheres. In cases where the silica layer was not needed, the RGD was layered directly onto the bare microspheres. Due to differences in the penetration of the osmium tetroxide stain through the layered particles, separate individual layers could not always be distinguished, but distinct differences in the structure and particle distribution can be seen with each added layer.

B. Iron-Oxide Nanoparticle-Based Microspheres as a Contrast Agent for MM-OCT and MRI

The addition of these protein microspheres (without magnetomotion) to a sample increases the nonspecific scattering in the OCT signal due to the oil core and high refractive index ($\sim$1.47) [26]. However, as the background scattering of the sample increases, it becomes increasingly difficult to distinguish the presence of these microspheres from the baseline optical scattering, and generating additional microsphere contrast (i.e., increase the differentiation between the microspheres and other structures) using magnetomotion becomes important. Fig. 2 shows results using a tissue-mimicking phantom prepared with TiO_2 as the background optical scattering particles in a 0.5% agarose gel. In the presence of a low concentration of TiO_2 (0.25 mg/mL), the increase in optical scattering is clearly visible in the OCT structural image (Fig. 2a). However, if the concentration of TiO_2 is increased (4 mg/mL), the change in optical scattering with the addition of microspheres is not immediately apparent, and magnetomotion can be used to increase the microsphere contrast (Figs. 2a and 2b). In the images without microspheres, structural OCT (red channel) dominates as the intensity of the green channel (MM-OCT signal) is negligible. In contrast, images with microspheres show an increased intensity in the green channel (laid on top of the red channel), suggesting the presence of stronger MM-OCT signal.

The source of magnetomotive contrast using only MNPs has been previously studied [27]. The sub-resolution MNPs are commonly bound to cell and tissue structures and when an external magnetic field gradient is applied, they move and displace these surrounding optical scatterers in the tissue microenvironment. Phase-resolved OCT measurements can be used to measure these small (nanometer to micrometer) displacements to enhance the contrast or probe the viscoelastic properties of the sample. These MNPs are known to provide a stiffness-dependent magnetomotive response that depends upon the elastic restoring force provided by the surrounding tissue. However, in samples that have low elastic restoring force (weak or not existent) the magnetomotive response will be relatively weak [27]. A dual-coil magnetomotive system has been developed that alternatively pulls the MNPs or magnetic microspheres in opposing directions, and enables magnetomotive OCT contrast in restoring-force-lacking liquids [13]. On the other hand, if the material is very stiff, the displacements will be less than the displacement sensitivity of the system ($<$10 nm), resulting again in a low magnetomotive signal [25].

Experiments with tissue-mimicking agarose phantoms were performed to explore the generating mechanism of the magnetomotive contrast from the nanoparticle-seeded microspheres. The agarose gel phantoms utilized in this study were tissue-mimicking in terms of both their optical and mechanical properties. Optically, TiO_2 (with concentration of 0.25–4 mg/ml) was added to the phantoms to increase the optical scattering properties to a comparable level to that of biological tissues. In fact, it has been reported that an addition of

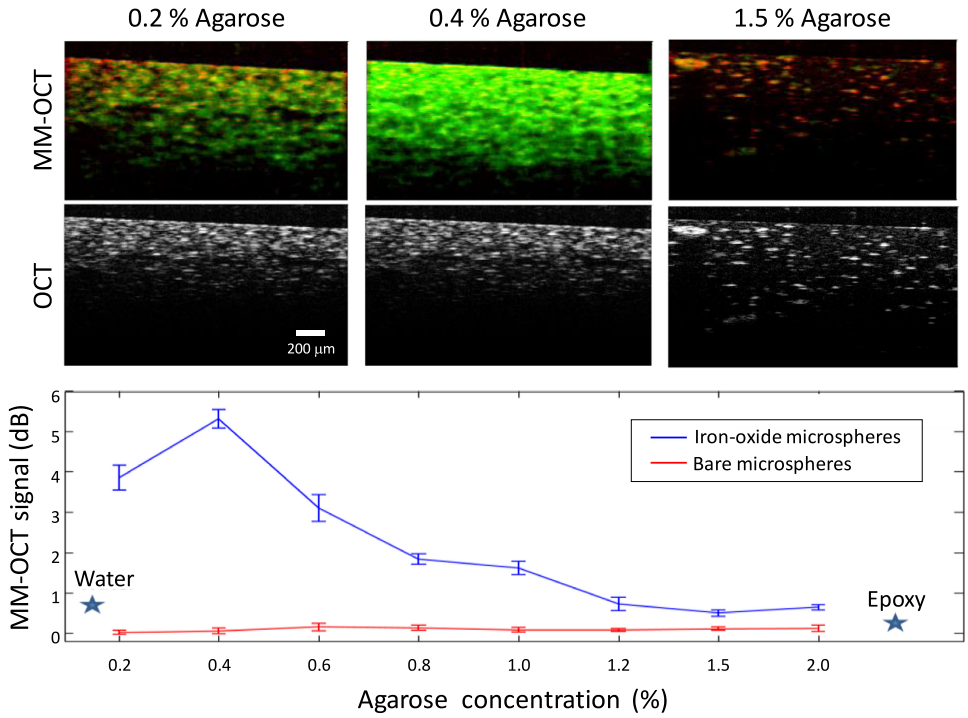

Fig. 3. The change in MM-OCT signal from nanoparticle-seeded microspheres in agarose phantoms of different stiffness. Upper panel: Representative images of structural OCT and corresponding MM-OCT in different concentrations of agarose gel. Bulk movement of microspheres generates contrast as the magnetomotive signal (green channel) depends on the viscoelastic properties of the medium. Lower panel: The MM-OCT signal decreases as the stiffness of the medium increases. The stars refer to the low MM-signal from the microspheres in water and embedded in epoxy.

a similar concentration of TiO_2 (0.25–2 mg/ml) to the optically transparent phantoms can increase the reduced optical scattering coefficient of the phantom to the same order of magnitudes of that of most biological tissues [28], [29]. Mechanically, agarose gels are produced to generate tissue-level elastic response. In this study, the produced Young's modulus (i.e., 4–52 kPa) of the agarose gel lies within the typical range of that of soft tissues, which is also the range of many phantom samples used in elastography [30]. MM-OCT using MNP-seeded microspheres can generate dynamic contrast either by the movement of the MNPs within their core, and/or the movement of the microspheres themselves. The concentration of the microspheres in the phantoms was kept constant while the stiffness of the surrounding gel was changed by varying the concentration of agarose. The range of stiffness varied between 4 kPa and 52 kPa, as measured by a spherical indentation measurement device (model TA.XT Plus Texture Analyzer, Texture Technologies Corp., Algonquin, IL). The stiffness-dependent change in the MM-OCT signal suggests that an elastic restoring force from the sample is required for higher magnetomotive contrast (Fig. 3). Furthermore, the decrease of magnetomotive signal at higher stiffness indicates that the magnetomotive response originates from the bulk movement of the microspheres. At the same time, the small signal in the stiffer samples shows that the movement of the MNPs inside the core (without the movement of the microspheres) by itself is small, and is not sufficient to generate strong magnetomotive contrast. In order to further validate this hypothesis, MM-OCT signal was measured from MNPs mixed only with vegetable oil and embedded in the epoxy (Fig. 3). The weak response supports the hypothesis that the main contribution of the magnetomotive signal is from the bulk movement of the microspheres rather than the nanoscale displacement of the MNPs within the core.

In the following experiments, the maximum effect of microspheres on the MM-OCT signal was explored by changing the concentration of microspheres in the sample and determining the encapsulation capacity of microspheres for iron oxide nanoparticles. MM-OCT was also evaluated for its capacity to quantify the concentration of microspheres to be able to provide information about their binding specificity and biodistribution in *in vitro* and *in vivo* experiments.

Different concentrations of microspheres (5.3×10^6–2.6×10^7 microspheres/ mL) produced with the same concentration of iron oxide (50 mg/mL in the oil solution) during their preparation, where embedded in 1% agarose gel. The volume of the microsphere suspension that was added to all samples was the same, and the assumption was made that the number of microspheres in the final samples would not significantly contribute to the overall gel stiffness. The MM-OCT signal intensity pixel values were averaged over the entire image and plotted as a function of the microsphere concentration (Fig. 4a). This plot shows positive correlation (Pearson's $r = 0.997$) between the microsphere concentration and the average magnetomotive intensity signals for samples at concentrations less than 1.5×10^7 microspheres/mL of gel. At concentrations greater than 1.5×10^7 microspheres/mL, the MM-OCT signal reached a plateau (MM-OCT signal of $\sim$ 4.5–5.5 dB). This plateau probably occurs when the amplitude of the displacement of the optical

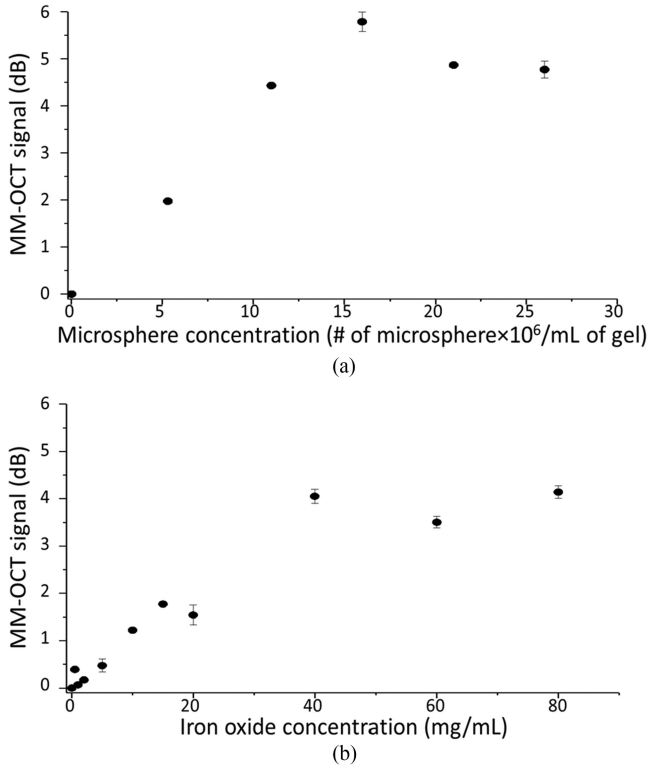

Fig. 4. (a) MM-OCT signal as a function of increasing microsphere concentration with a constant iron oxide concentration in the oil solution during microsphere synthesis. Average MM-OCT signal was calculated by averaging the MM-OCT signal across all pixels in the image. (b) MM-OCT signal as a function of increasing iron oxide concentration in the oil solution during microsphere synthesis. Microspheres were embedded in a 1% agarose gel at a concentration of 10^7/mL of gel.

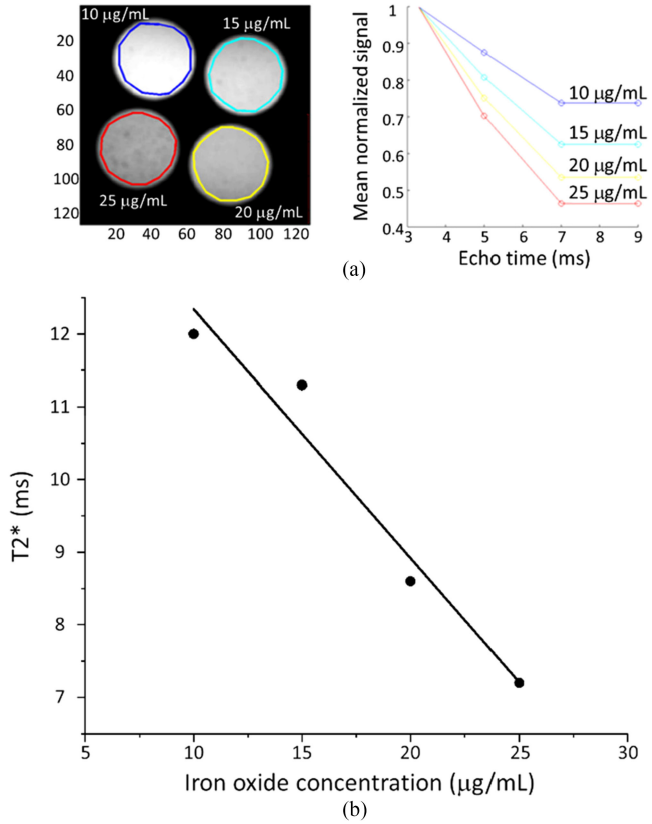

Fig. 5. (a) MRI measurements of agarose gels with increasing concentrations of iron oxide. Left: a representative MRI slice through capillary tubes containing agarose gel with iron oxide MNPs. Right: plots of the mean normalized MRI signal from the 19 images taken at four echo times for different concentrations of iron oxide. The color of the slice boundaries on the left image correspond to the plots with the same iron oxide concentrations. (b) T2* relaxation time as a function of non-encapsulated iron oxide concentration in the agarose gel.

scatterer, as the magnetic field is modulated, is large enough that the measured optical phase changes by more than π [9]. In this case, it is not possible to properly unwrap the optical phase, however, for strong optical scatterers and large displacements, it may be possible to use changes in the amplitude of the MM-OCT signal, rather than the more sensitive phase-based measurement.

In a separate experiment, microspheres were prepared in oil stock solutions with increasing iron oxide concentrations from 0 to 80 mg/mL, and 1.0×10^7 microspheres were used for each sample. The MM-OCT signal increased linearly with increasing encapsulated nanoparticle concentrations up to about 40 mg of iron oxide/mL of oil of the stock solution at the time of synthesis (Fig. 4b). At higher concentrations, the average magnetomotive signal began to plateau, suggesting the maximum amount of iron oxide nanoparticles that could be encapsulated into these particular protein microspheres was reached, or that the phase wrapping of the imaging system occurred. Thus, it was necessary to quantify the optimal amount of iron oxide encapsulated in the microspheres.

Superparamagnetic iron oxide (SPIO) nanoparticles have been extensively studied as MRI contrast agents both *in vitro* and *in vivo* for cancer applications [31]–[34]. For our MRI studies, the iron oxide nanoparticles in oil, or the iron oxide-filled protein microspheres, were suspended in 1% low melting agarose gels and solidified in capillary tubes. To reduce the formation of air bubbles and the potential settling of microspheres that would cause non-homogenous samples, the capillary tubes were vortexed and placed into a water bath at room temperature to facilitate a rapid and uniform solidification process. The MRI measurements were taken at four different echo times of 3.3 ms, 5.0 ms, 7.0 ms, and 9.0 ms, and nineteen MRI slices were taken throughout the full volume of the gel in the capillary tubes. A standard curve was created using the MRI measurements from agarose gels with increasing concentrations of iron oxide nanoparticles (10–25 μg/mL) in the agarose gel (Fig. 5a). The mean MRI signals as a function of the echo times were plotted (Fig. 5a) to extract the relaxation times (T2*) using a Matlab script. The obtained T2* values clearly show a linear correlation (Pearson's $r = -0.98$) with the concentration of iron oxide (Fig. 5b).

A similar experiment using increasing concentrations of iron oxide-filled microspheres was performed to optimize the microsphere concentration for the MRI imaging. Based on the results of our previous study with sufficient MRI signal levels, [10], agarose gels were made with increasing concentrations of microspheres from 6.6×10^5 to 2.6×10^6 microspheres/mL and prepared with an oil stock iron oxide concentration of 15.0 mg/mL. The T2* values also show a linear correlation (Pearson's $r = -0.986$) with the concentration of microspheres (Fig. 6). The concentration of 2.0×10^6 microspheres/mL was

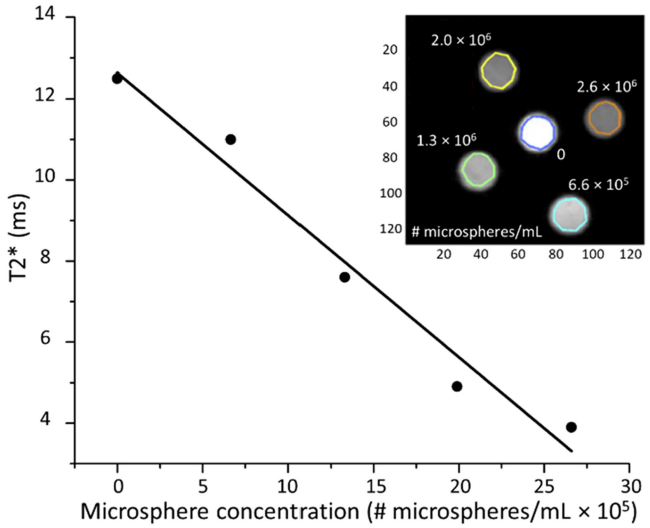

Fig. 6. T2* relaxation time measured as a function of microsphere concentration with a constant iron oxide concentration (15 mg/mL) in the oil solution during microsphere synthesis. Microspheres were embedded in a 1% agarose gel. T2* values were obtained from the plots of the mean normalized MRI signal from the 19 images taken at four echo times as presented in Fig. 5. Inset: a representative MRI slice through the capillary tubes containing agarose gel with different concentrations of microspheres.

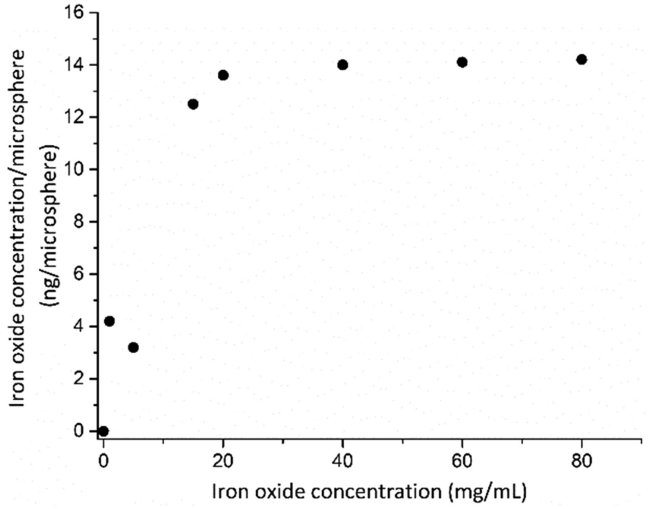

Fig. 7. The dependence of the iron oxide concentration in the microspheres on the initial concentration of iron oxide in the oil stock solution during the synthesis of protein microspheres. Concentration of iron oxide in the microspheres is calculated from the measured T2* values and the standard curve obtained with non-encapsulated iron oxide concentration in the agarose gel (Fig. 5).

chosen to determine the amount of iron oxide encapsulated in the microspheres. Using the iron oxide concentration standard curve (Fig. 5), the total iron oxide concentrations were calculated from the T2* values and divided with the concentration of microspheres measured with the DLS instrument. As the concentration of iron oxide in the oil stock solution was increased (up to 20 mg/mL), the amount of iron oxide per microsphere was also increased (Fig. 7). However, when the concentration of iron oxide in the oil solution during the preparation was increased above 20 mg/mL, the T2* values were not significantly changing (Fig. 7). Interestingly, these findings agree with the MM-OCT results in Fig. 4b, which found the maximum average

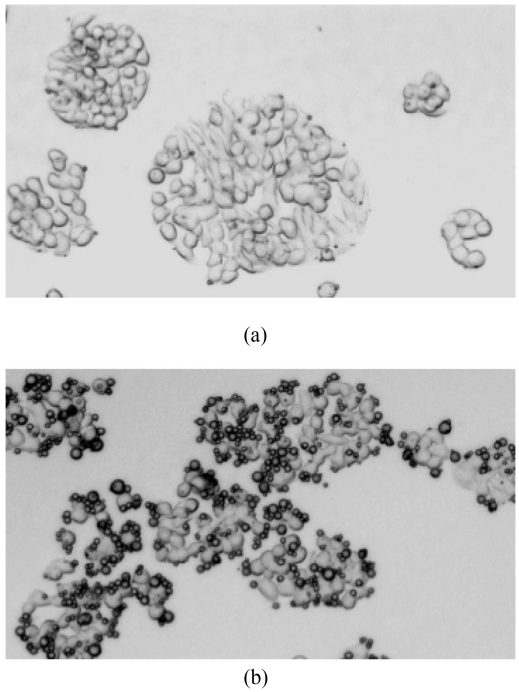

Fig. 8. Brightfield images of HT-29 cells at 10X after they have been incubated for two hours with (a) non-targeted and (b) RGD-targeted protein microspheres.

magnetomotive OCT signal/microsphere reaching a plateau for microspheres made with iron oxide oil stock concentrations greater than 20–40 mg/mL. This phenomenon can be explained by the achievement of either the saturation of the imaging modalities or the upper limit for encapsulating iron oxide nanoparticles into the protein microspheres. Further confirmation of the amount of iron oxide nanoparticles in the microspheres should be obtained from mass spectroscopy measurements.

C. In Vitro *Targeting of Cancer Cells*

In addition to multimodal imaging, the use of core-shell particles and capsules such as liposomes, protein microspheres, polymer micelles, and dendrimers is advantageous for targeted drug delivery applications [11], [14], [35]. The binding specificity and affinity of protein microspheres for specific binding was tested by attaching RGD peptide to selectively target $\alpha_v\beta_3$ integrin receptors, which are often overexpressed on metastatic cancer cells, in angiogenesis, and in atherosclerosis. In preliminary experiments, the RGD-functionalized and non-functionalized microspheres were incubated with HT-29 cancer cells for two hours and washed with PBS to remove any excess of unbound microspheres. This human colon cancer cell line is well-known to overexpress the $\alpha_v\beta_3$ integrin receptor [36], [37]. The light microscopy images (Fig. 8) confirmed the previously reported results [12]. The higher binding affinity of the RGD-functionalized protein microspheres to the HT-29 cells can be clearly seen when compared to the non-functionalized protein microspheres.

Absolute quantification of $\alpha_v\beta_3$ integrin receptors expressed on the cell surface can be measured by flow cytometry of cells labeled with fluorochrome-coupled monoclonal antibodies specific to the alpha and beta subunits of the integrin receptor.

However, this method cannot be directly used to evaluate binding of the protein microspheres to these receptors, and it may be more relevant to compare relative trends between different cell lines. First, SEM images of RGD-functionalized protein microspheres showed that the microspheres do not appear to be uniformly and completely coated with RGD peptides (Fig. 1), so that the orientation of the microspheres relative to the binding sites is not always well matched. In addition, the overall size of these microspheres (1–3 μm) is relatively large compared to monoclonal antibodies ($\sim$5–10 nm) and the average cell size (10–15 μm). This size difference would physically constrain access of microspheres to bind nearby integrin receptors exposed on the cell surface. On the other hand, compared to fluorescence microscopy, which examines cells that are attached to the bottom of Petri dishes, the entire cell surface is exposed during flow cytometry. The significant populations of integrin receptors, which mediate cell-substrate adhesion, are likely present at the junction between the cells and the bottom of the culture dish, rather than on the apical side of the cells, which is what is exposed for the interaction with microspheres. Given all of these factors, microsphere binding can measure only the relative expression of the integrin receptors on the cell surface or compare the relative affinities of the receptor binding between different cell lines.

Seven cancer cell lines (Table I) with different levels of $\alpha_v\beta_3$ integrin expression were prepared for flow cytometry by adding the primary $\alpha_v\beta_3$ antibody (mouse monoclonal IgG1, GeneTex cat. #GTX4013) to label the exposed $\alpha_v\beta_3$ integrin receptors on the cell surface (positive staining). The MCF-7 cell line was chosen as a negative control since it has a low or no expression of the $\alpha_v\beta_3$ integrin receptor, while the MDA-MB-231 and MDA-MB-435S cell lines are highly metastatic breast cancer cell lines overexpressing the $\alpha_v\beta_3$ receptor [38]. The secondary antibody (anti-mouse conjugated with FITC) was added to both labeled cells and negative controls. Although the flow cytometry data can give the actual number of integrin molecules per each cell, in this study they were expressed as the ratio of specific binding (difference between positively and negatively stained cells) to non-specific binding (negatively stained cells) (Fig. 9b) to more easily compare the results from flow cytometry with the fluorescence microscopy targeting data with the RGD-functionalized microspheres (Fig. 9a). The binding specificity of Nile Red-filled microspheres to the cancer cells was quantified using fluorescence microscopy.

Approximately 10^5 cells from each cancer cell line were seeded into each well of a 4-well chamber slide. For each cell line, two of the four wells were incubated with RGD-functionalized Nile Red-filled microspheres and the other two wells were incubated with non-functionalized Nile Red-filled microspheres. All wells were incubated with $\sim$40,000 microspheres for 1 hour. The fluorescence images were overlaid on top of their respective brightfield images to better visualize the localization of Nile Red dye. The fluorescence intensity signals from the rescaled images were averaged over the entire image using ImageJ software (NIH, Version 1.45) and ten images were averaged for each cell type. The percent increase in fluorescence calculated by comparing average fluorescence intensities of RGD-functionalized vs. non-functionalized

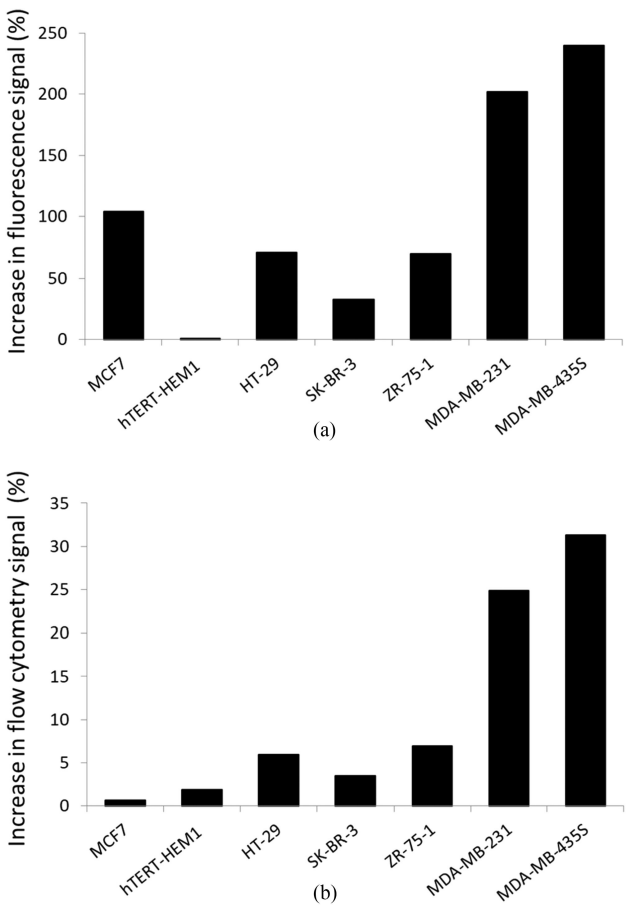

Fig. 9. (a) Increase in the average fluorescence intensity of cells incubated with RGD-coated microspheres compared to cells incubated with microspheres with no RGD attached, measured by fluorescence microscopy. (b) Increase in flow cytometry signal from stained cells compared to the control cells. Flow cytometry results for the $\alpha_v\beta_3$ integrin receptor expression shows a similar trend as fluorescence imaging data for the same cell lines.

microspheres bound to each cell line correlated closely (Pearson's $r = 0.921$) with the flow cytometry results (Fig. 9). The two metastatic cell lines (MDA-MB-231 and MDA-MB-435S) that have the highest expression of surface integrin receptors measured by flow cytometry were also bound with the highest number of RGD-functionalized microspheres as determined by fluorescence imaging. While preliminary trend could be observed, any statistical significance still needs to be established.

In this study diffuse fluorescent dye was observed across the surface area of the cell, which suggested cellular uptake and degradation of the protein microspheres by the cancer cells. Several published reports indicate that the ligands bound to the $\alpha_v\beta_3$ integrin receptor may induce endocytosis [39], [40]. Due to the size of the microspheres, the nonspecific staining of the entire cell by the Nile Red, and the binding of the microsphere by the cell via the $\alpha_v\beta_3$ integrin receptor, the most likely method of cellular uptake of the microspheres is endocytosis. According to another study, LBL particles up to several micrometers in size were internalized by epithelial cells, monocytes, and dendritic cells by endocytosis [41].

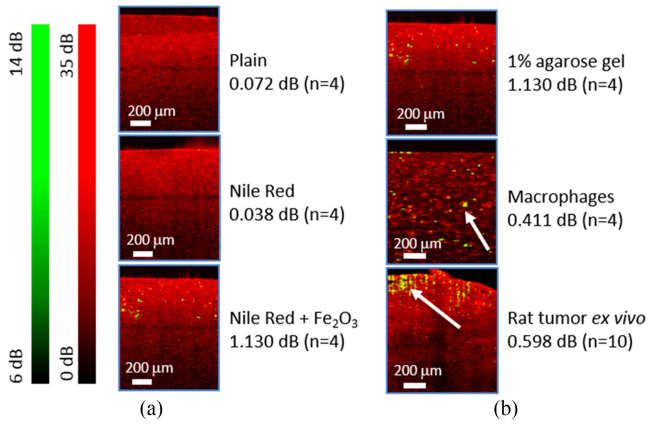

Fig. 10. MM-OCT of microspheres. (a) Different types of microspheres in the same environment, and (b) iron-oxide-filled microspheres in different scattering environments. (a) Top: microspheres with only an oil core; middle: microspheres with Nile Red; bottom: microspheres with iron oxide nanoparticles and Nile Red. All microspheres were embedded in 1% agarose gel for MM-OCT imaging. A representative MM-OCT image for each condition is shown, and the average amplitude change of the magnetic signal over an entire image is reported. (b) Top: Microspheres with iron oxide and Nile Red embedded in agarose gel; middle: macrophages incubated with the same microspheres, and after 4 hours, embedded in agarose gel; bottom: tumors from an NMU-mammary cancer rat model were excised and injected *ex vivo* with 10^5 microspheres. Representative MM-OCT images for each condition are shown and the average amplitude change of the magnetic signal over an entire image is reported. Arrows: embedded microspheres.

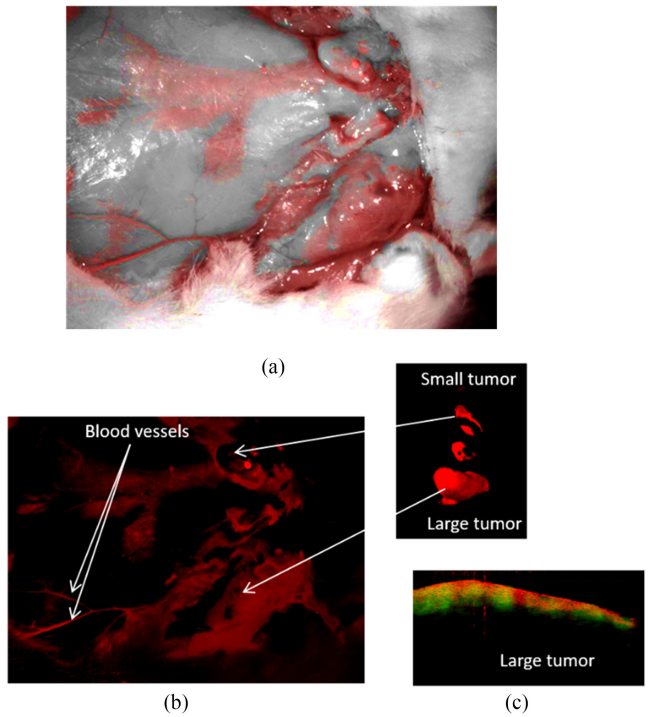

Fig. 11. *In vivo* rat mammary tumor targeting. Microspheres with iron oxide and Nile Red were functionalized with RGD, and $\sim 10^9$ microspheres were injected through the jugular vein. After 30 minutes, the rat was euthanized and dissected tumors were imaged in a fluorescence-imaging darkbox and with MM-OCT. (a) Overlay of brightfield and fluorescence images of the exposed tumors. Blood vessels leading to and around small and big tumors are visible due to the presence of Nile Red–filled microspheres in the blood circulation. (b) Fluorescence images with arrows indicating the locations of the small and large tumors, and surrounding blood vessels. Inset: Fluorescence images of excised tumors. (c) MM-OCT image shows strong signal (green channel) in the large excised tumor, confirming the presence of targeted microspheres.

D. MM-OCT Imaging in Different Biological Environments

Further attempts were made to investigate the difference in magnetomotive signal of nanoparticle-seeded microspheres in different biological environments. In the control experiment, three different batches of microspheres were produced: 1) with only an oil core (plain), 2) with Nile Red in the oil core, and 3) with iron oxide nanoparticles and Nile red in the oil core. Microspheres were embedded in 1% agarose gel for MM-OCT imaging. The average amplitude change of the magnetic signal over an entire image (expressed as mean dB) was ~10–30x lower for both the plain and Nile red microspheres (0.072 dB and 0.038 dB, respectively) compared to the microspheres with nanoparticles (1.130 dB; Fig. 10a), which if quantified without logarithmic expression, corresponds to ~30% difference. These preliminary results show that higher MMOCT signals are present in the nanoparticle-laden microspheres indicates that the magnetomotive signal likely originated only from the iron oxide component of the microspheres. Further studies are required to confirm statistical significance. These microspheres were then used to compare magnetomotive signal in different biological environments. One batch of microspheres was incubated with macrophages for 4 hours, after which macrophages were washed and embedded in the agarose gel. The other batch of microspheres was injected in an excised tumor from an NMU-induced mammary tumor rat model [42], [43]. The MM-OCT images clearly show magnetomotive signal from microspheres within macrophages (Fig. 10b, middle) and tumor (Fig. 10b, bottom). The results of this experiment demonstrate the ability of MM-OCT to record signal from iron oxide-filled microspheres in both low optical scattering and high optical scattering environments. Although statistical significance testing has not been performed, the observation of the presence of a lower signal obtained from the rat tumor (0.598 dB) and macrophages (0.411 dB), compared to the microspheres directly embedded in the agarose gel (1.130 dB), is still worth noting. This could be explained by differences in the stiffness of the microenvironment. Although the same concentration of microspheres (10^5) was used in all three tests, the concentration of internalized microspheres depends on the endocytotic activity and is very likely lower than the concentration injected into the tumor and embedded in the agarose. On the other hand, lower MM-OCT signal from the tumor could be influenced by the tissue heterogeneity.

E. In Vivo *Targeting in a Pre-Clinical Cancer Model*

Preliminary results demonstrated that RGD-functionalized protein microspheres can be used as a multimodal contrast agent for targeting spontaneous mammary tumors in rats [10]. In this study, we used a well-characterized N-methyl-N-nitrosourea (NMU)-induced rat mammary tumor model, which has been shown to most closely mimic the natural development and progression of human breast tumors, notably ductal carcinoma *in situ*. Microspheres with iron oxide nanoparticles and Nile Red were functionalized with RGD, and $\sim 10^9$ microspheres

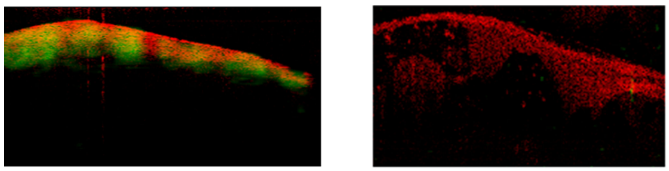

(a) Tumor with targeted microspheres (b) Tumor with non-targeted microspheres

Fig. 12. Conformation of tumor targeting by microspheres. Rats were injected with either functionalized or non-functionalized microspheres (without RGD), and euthanized after 30 minutes. (a) MM-OCTsignal in the dissected tumor injected with the targeted microspheres compared to (b) the tumor injected with nontargeted microspheres, confirms the presence of targeted microspheres.

were injected through the jugular vein. After 30 minutes, the rat was euthanized and dissected tumors were imaged to obtain both MM-OCT and fluorescence signals (Fig. 11). Strong MM-OCT signal was recorded from both tumors that were present (data shown only for the larger tumor; Fig. 11c). In addition, fluorescence signal from Nile Red is clearly visible in the blood vessels surrounding the tumors, indicating the binding of microspheres to $\alpha_v\beta_3$ integrin receptors that are overexpressed during angiogenesis around these tumors.

In the control experiment, rats were injected with non-targeted microspheres. The MM-OCT images verify the ability of targeted microspheres to specifically target tumors (Fig. 12).

V. Conclusion

The trend in biomedical imaging is toward early detection and diagnosis of disease. Since virtually all diseases originate at the molecular and cellular level, detection and imaging systems with resolutions and sensitivities capable of imaging at these levels would be most valuable. OCT is a high-resolution biomedical imaging modality that has the potential for applications in a large number of medical and surgical fields, including ophthalmology, cardiology, and oncology. This study describes the development, characterization, and application of targeted nanoparticle-seeded protein microspheres that can provide magnetomotive and magnetic resonance imaging contrast. The majority of the optical probes developed in recent years have been based on the emission of a bioluminescent or fluorescent signal. While these methods now have an established track record of use, there remains a number of other optical imaging methods that would equally benefit from novel optical agents that could not only non-specifically enhance contrast within images, but ultimately provide the same molecular specificity afforded by the bioluminescent and fluorescent probes through site-specific molecular targeting.

Although imaging data demonstrated that magnetic microspheres functionalized with linear RGD were effectively binding to cancer cells expressing high levels of the $\alpha_v\beta_3$ integrin receptors, non-specific binding was also present. In order to improve these targeting capabilities, additional research needs to be performed to increase the level of specific binding, for example by using cyclic RGD instead of the linear form. Studies suggest that cyclic RGD has a higher binding specificity and affinity for the $\alpha_v\beta_3$ integrin receptor than linear RGD [44]–[48], and also may increase the circulation lifetime of the carrier. Cyclic RGD was not as quickly degraded and cleared from the body as linear RGD [44]–[48].

Before any major studies are undertaken to explore the use of nanoparticle-seeded protein microspheres as therapeutic agents, further *in vitro* and *in vivo* work should be performed to study their biodistribution and mechanism of cellular uptake. Cellular uptake and degradation of microspheres enabling the release of encapsulated therapeutic agents would be desired in applications where diseased cells are targeted; however, for imaging purposes in which the microspheres serve as contrast agents, destruction of the microspheres would limit their practical use.

Preliminary results support the hypothesis that multifunctional nanoparticle-based microspheres targeted to the $\alpha_v\beta_3$ integrin can provide molecularly-sensitive contrast in MM-OCT for detection, but at the same time could have the therapeutic potential for the local delivery of encapsulated lipophilic drugs or heat absorbing particles to induce hyperthermia. The possibility of controlling the *in vivo* rupture of microspheres to release its shell or core contents is a promising application of these agents as a means for drug administration as well as delivery of genetic material and proteins [10], [11], [14], [35]. These targeted protein microspheres would therefore serve as potential site-specific drug delivery vehicles with relatively high drug carrying capacity. It was shown that an alternating magnetic field can be used to heat MNPs, causing a local increase in tissue temperature [49]–[53]. This magnetic hyperthermia can further induce cell apoptosis in cancer cells if they are heated between 41–46 °C, or even induce necrotic cell death if heated over 46 °C [54]. Further studies should be conducted to explore whether magnetic hyperthermia induced by the encapsulated MNPs could potentially rupture the microspheres and release the core content, or induce thermal damage to targeted cancerous cells.

References

[1] E. A. Swanson *et al.*, "Optical coherence tomography: Principles, instrumentation, and biological applications," in *Biomedical Optical Instrumentation and Laser-Assisted Biotechnology*, A. M. Scheggi, S. Martellucci, A. N. Chester, and R. Pratesi, Eds., 1st ed. Dordrecht, The Netherlands: Kluwer, 1996, pp. 291–305.

[2] A. Zysk and S. A. Boppart, "Optical coherence tomography," in *Techniques and Advanced Systems*, P. Torok and F. J. Kao, Eds., 2nd ed. Berlin, Germany: Springer-Verlag, 2007, pp. 401–437.

[3] S. A. Boppart, A. L. Oldenburg, C. Xu, and D. L. Marks, "Optical probes and techniques for molecular contrast enhancement in coherence imaging," *J. Biomed. Opt.*, vol. 10, 2005, Art. no. 41208.

[4] R. John *et al.*, "*In vivo* magnetomotive optical molecular imaging using targeted magnetic nanoprobes," *Proc. Nat. Acad. Sci. USA*, vol. 107, pp. 8085–8090, 2010.

[5] R. John and S. A. Boppart, "Magnetomotive molecular nanoprobes," *Curr. Med. Chem.*, vol. 18, pp. 2103–2114, 2011.

[6] A. L. Oldenburg, J. R. Gunther, and S. A. Boppart, "Imaging magnetically labeled cells with magnetomotive optical coherence tomography," *Opt. Lett.*, vol. 30, no. 7, pp. 747–749, 2005.

[7] V. Crecea, A. L. Oldenburg, X. Liang, T. S. Ralston, and S. A. Boppart, "Magnetomotive nanoparticle transducers for optical rheology of viscoelastic materials," *Opt. Express*, vol. 17, pp. 23114–23122, 2009.

[8] X. Liang and S. A. Boppart, "Biomechanical properties of *in vivo* human skin by dynamic optical coherence elastography," *IEEE Trans. Biomed. Eng.*, vol. 57, no. 4, pp. 953–959, Apr. 2010.

[9] A. L. Oldenburg, V. Crecea, S. A. Rinne, and S. A. Boppart, "Phase-resolved magnetomotive OCT for imaging nanomolar concentrations of magnetic nanoparticles in tissues," *Opt. Express*, vol. 16, pp. 11525–11539, 2008.

[10] R. John *et al.*, "Targeted multi-functional multi-modal protein-shell microspheres as cancer imaging contrast agents," *Mol. Imag. Biol.*, vol. 14, pp. 17–24, 2011.
[11] B. Zhang, J. Xing, and H. Liu, "Preparation and application of magnetic microsphere carriers," *Front. Chem. Eng. China*, vol. 1, pp. 96–101, 2007.
[12] F. J. Toublan, S. A. Boppart, and K. S. Suslick, "Tumor targeting by surface-modified microspheres," *J. Amer. Chem. Soc.*, vol. 128, pp. 3472–3473, 2006.
[13] J. Kim *et al.*, "Intravascular magnetomotive optical coherence tomography of targeted early-stage atherosclerotic changes in *ex vivo* hyperlipidemic rabbit aortas," *J. Biophoton.*, vol. 9, pp. 109–116, 2016.
[14] O. Grinberg, M. Hayun, B. Sredni, and A. Gedanken, "Characterization and activity of sonochemically-prepared BSA microspheres containing Taxol – Anticancer drug," *Ultrason. Sonochem.*, vol. 14, pp. 661–666, 2007.
[15] R. Dijkhuizen-Radersma, S. C. Hesseling, P. E. Kaim, K. de Groot, and J. M. Bezemer, "Biocompatibility and degradation of poly(ether-ester) microspheres: In vitro and in vivo evaluation," *Biomaterials*, vol. 23, no. 24, pp. 4719–4729, 2002.
[16] H. Xiang, Y. Mu, C. Hu, and X. Luo, "Biocompatibility and toxicity of polylactic acid/ferrosoferic oxide nanomagnetic microspheres," *J. Nanomater.*, vol. 4, pp. 1–8, 2017.
[17] K. S. Suslick and M. W. Grinstaff, "Protein microcapsulation of nonaqueous liquids," *J. Amer. Chem. Soc.*, vol. 112, pp. 7807–7809, 1990.
[18] M. W. Grinstaff and K. S. Suslick, "Nonaqueous liquid filled microcapsules," *Polym. Preprints*, vol. 32, pp. 255–256, 1991.
[19] A. G. Webb *et al.*, "Sonochemically produced fluorocarbon microspheres: A new class of MRI contrast agents," *J. Magn. Reson. Imag.*, vol. 6, pp. 675–683, 1996.
[20] J. Lohrke *et al.*, "25 Years of contrast-enhanced MRI: Developments, current challenges and future perspectives," *Adv. Therapy*, vol. 33, pp. 1–28, 2016.
[21] M. R. Bashir, T. A. Jaffe, T. V. Brennan, U. D. Patel, and M. J. Ellis, "Renal transplant imaging using magnetic resonance angiography with a nonnephrotoxic contrast agent," *Transplantation*, vol. 96, pp. 91–96, 2013.
[22] E. Ruoslahti, "Fibronectin and its integrin receptors in cancer," *Adv. Cancer Res.*, vol. 76, pp. 1–20, 1999.
[23] R. Pasqualini, E. Koivunen, and E. Ruoslahti, "Alpha v integrins as receptors for tumor targeting by circulating ligands," *Nature Biotechnol.*, vol. 15, pp. 542–546, 1997.
[24] P. M. Winter *et al.*, "Molecular imaging of angiogenesis in early-stage atherosclerosis with $\alpha_{\rm v}\beta_3$ integrin-targeted nanoparticles," *Circulation*, vol. 108, pp. 2270–2274, 2003.
[25] C. Burtea *et al.*, "Molecular imaging of $\alpha_{\rm v}\beta_3$ integrin expression in atherosclerotic plaques with a mimetic of RGD peptide grafted to Gd-DTPA," *Cardiovasc. Res.*, vol. 78, pp. 148–157, 2008.
[26] T. M. Lee *et al.*, "Engineered microsphere contrast agents for optical coherence tomography," *Opt. Lett.*, vol. 28, pp. 1546–1548, 2003.
[27] R. John, E. J. Chaney, and S. A. Boppart, "Dynamics of magnetic nanoparticle-based contrast agents in tissues tracked using magnetomotive optical coherence tomography," *IEEE J. Sel. Top. Quantum Electron.*, vol. 16, no. 3, pp. 691–697, May/Jun. 2010.
[28] M. Fonseca, B. Zeqiri, P. Beard, and B. Cox, "Characterisation of a phantom for multiwavelength quantitative photoacoustic imaging," *Phys. Med. Biol.*, vol. 61, pp. 4950–4973, 2016.
[29] S. L. Jacques, "Optical properties of biological tissues: A review," *Phys. Med. Biol.*, vol. 58, pp. R37–R61, 2013.
[30] T. J. Hall, M. Bilgen, M. F. Insana, and T. A. Krouskop, "Phantom materials for elastography," *IEEE Trans. Ultrason., Ferroelectr., Freq. Control*, vol. 44, no. 6, pp. 1355–1365, Nov. 1997.
[31] X. H. Peng *et al.*, "Targeted magnetic iron oxide nanoparticles for tumor imaging and therapy," *Int. J. Nanomed.*, vol. 3, pp. 311–321, 2008.
[32] H. B. Na, I. C. Song, and T. Hyeon, "Inorganic nanoparticles for MRI contrast agents," *Adv. Mater.*, vol. 21, pp. 2133–2148, 2009.
[33] J. W. Bulte and D. L. Kraitchman, "Iron oxide MR contrast agents for molecular and cellular imaging," *NMR Biomed.*, vol. 17, pp. 484–499, 2004.
[34] S. Laurent, J. L. Bridot, L. V. Elst, and R. N. Muller, "Magnetic iron oxide nanoparticles for biomedical application," *Future Med. Chem.*, vol. 2, pp. 427–449, 2010.
[35] O. Grinberg *et al.*, "Sonochemically prepared BSA microspheres containing Gemcitabine, and their potential application in renal cancer therapeutics," *Acta Biomater.*, vol. 5, pp. 3031–3037, 2009.
[36] N. Reinmuth *et al.*, "$\alpha_{\rm v}\beta_3$ integrin antagonist S247 decreases colon cancer metastasis and angiogenesis and improves survival in mice," *Cancer Res.*, vol. 63, pp. 2079–2087, 2003.
[37] J. Laferriere, F. Houle, and J. Huot, "Adhesion of HT-29 colon carcinoma cells to endothelial cells requires sequential events involving E-selectin and integrin β_4," *Clin. Exp. Metastasis*, vol. 21, pp. 257–264, 2004.
[38] A. Taherian, X. Li, Y. Liu, and T. A. Haas, "Differences in integrin expression and signaling within human breast cancer cells," *BMC Cancer*, vol. 11, 2011, Art. no. 293.
[39] F. Danhier, A. Le Breton, and V. Preat, "RGD-based strategies to target alpha(v) beta(3) integrin in cancer therapy and diagnosis," *Mol. Pharmaceutics*, vol. 9, pp. 2961–2973, 2012.
[40] L. Sancey *et al.*, "Clustering and internalization of integrin alpha(v) beta(3) with a tetrameric RGD-synthetic peptide," *Mol. Therapy*, vol. 17, pp. 837–843, 2009.
[41] Y. Yan, S. K. Such, A. P. Johnston, H. Lomas, and F. Caruso, "Toward therapeutic delivery with layer-by-layer engineered particles," *ACS Nano*, vol. 5, pp. 4252–4257, 2011.
[42] J. Russo and I. H. Russo, "Experimentally induced mammary tumors in rats," *Breast Cancer Res. Treatment*, vol. 39, pp. 7–20, 1996.
[43] H. J. Thompson, M. Singh, and J. McGinley, "Rat models of premalignant breast disease," *J. Mammary Gland Biol. Neoplasia*, vol. 5, pp. 409–420, 2000.
[44] M. Fani *et al.*, "Comparative evaluation of linear and cyclic 99mTc-RGD peptides for targeting of integrins in tumor angiogenesis," *Anticancer Res.*, vol. 26, pp. 431–434, 2006.
[45] S. Liu, "Radiolabeled cyclic RGD peptides as integrin $\alpha_{\rm v}\beta_3$-targeted radiotracers: Maximizing binding affinity via bivalency," *Bioconjugate Chem.*, vol. 20, pp. 2199–2213, 2009.
[46] Y. Zhou, S. Chakraborty, and S. Liu, "Radiolabeled cyclic RGD peptides as radiotracers for imaging tumors and thrombosis by SPECT," *Theranostics*, vol. 1, pp. 58–82, 2011.
[47] S. Liu, "Radiolabeled multimeric cyclic RGD peptides as integrin $\alpha_{\rm v}\beta_3$ targeted radiotracers for tumor imaging," *Mol. Pharmaceutics*, vol. 3, pp. 472–487, 2006.
[48] J. Li *et al.*, "Enhancement and wavelength-shifted emission of Cerenkov luminescence using multifunctional microspheres," *Phys. Med. Biol.*, vol. 60, pp. 727–739, 2015.
[49] M. Johannsen *et al.*, "Magnetic fluid hyperthermia (MFH) reduces prostate cancer growth in the orthotopic Dunning R3327 rat model," *Prostate*, vol. 64, pp. 283–292, 2005.
[50] K. Maier-Hauff *et al.*, "Intracranial thermotherapy using magnetic nanoparticles combined with external beam radiotherapy: Results of a feasibility study on patients with glioblastoma multiforme," *J. Neuro-Oncol.*, vol. 81, pp. 53–60, 2007.
[51] T. G. Murray *et al.*, "Ferromagnetic hyperthermia: Functional and histopathologic effects on normal rabbit ocular tissue," *Int. J. Hyperthermia*, vol. 13, pp. 423–436, 1997.
[52] A. Jordan *et al.*, "Effects of fluid hyperthermia (MFH) on C3H mammary carcinoma *in vivo*," *Int. J. Hyperthermia*, vol. 13, pp. 587–605, 1997.
[53] D. Kenneth *et al.*, "Epithelial internalization of supermagnetic nanoparticles and response to external magnetic field," *Biomaterials*, vol. 26, pp. 2061–2072, 2005.
[54] I. Hilger *et al.*, "Electromagnetic heating of breast tumors in interventional radiology: *In vitro* and *in vivo* studies in human cadavers and mice," *Radiology*, vol. 218, pp. 570–575, 2001.

Marina Marjanovic received the B.S. degree in molecular biology and physiology in 1979, the M.S. and Ph.D. degrees in physiology in 1987 and 1992, respectively, from the University of Belgrade, Belgrade, Serbia. She was a Postdoctoral Fellow with the University of Illinois at Urbana-Champaign, Champaign, IL, USA, from 1992 to 1996. In 1996, she accepted a faculty position with the Eastern Illinois University, Charleston, IL, USA. In 2009, she returned to the University of Illinois at Urbana-Champaign, where she is currently a Teaching Associate Professor with the Department of Bioengineering and the Associate Director of the Center for Optical Molecular Imaging. She authored and co-authored 5 book chapters, 47 peer-reviewed publications, 64 presentations with published proceedings, and 62 meeting presentations. Her research interests include translational studies using novel imaging technologies.

Freddy T. Nguyen received the B.S. degree in chemistry and the B.A. degree in mathematics from Rice University, Houston, TX, USA, in 2002, and the Ph.D. and M.D. degrees from the University of Illinois at Urbana-Champaign, Champaign, IL, USA, in 2015 and 2016, respectively. He is currently an Arnold O. Beckman Postdoctoral Fellow with the Massachusetts Institute of Technology, Cambridge, MA, USA. He is a Member of the American Medical Association, the American Association for the Advancement of Science, the American Association for Cancer Research, and the American Chemical Society. His graduate research interests broadly include the development of spectroscopic and imaging techniques and their associated contrast agents for direct biomedical applications.

Adeel Ahmad received the B.S. degree from the National University of Sciences and Technology, Karachi, Pakistan, in 2006, and the M.S. and Ph.D. degrees from the University of Illinois at Urbana-Champaign, Champaign, IL, USA, in 2010 and 2014, respectively, all in electrical engineering. In his graduate research, he worked on utilizing magnetic particles for contrast enhancement in optical imagining and elastography application.

Pin-Chieh Huang received the B.S. degree in electrophysics from the National Chiao Tung University, Hsinchu, Taiwan, in 2013, and the M.S. degree in bioengineering in 2016 from the University of Illinois at Urbana-Champaign, Champaign, IL, USA, where she is currently working toward the Ph.D. degree in bioengineering. Her research interests include optical coherence tomography and elastography.

Kenneth S. Suslick the B.S. degree from the California Institute of Technology, Pasadena, CA, USA, in 1974, and the Ph.D. degree from Stanford University, Stanford, CA, USA, in 1978.

Thereafter, he immediately came to the University of Illinois at Urbana-Champaign, Champaign, IL, USA, where he is a Professor with the Department of Chemistry. He has authored or co-authored more than 397 papers, edited four books, and holds 48 patents and patent applications. His three major research interests include the chemical effects of ultrasound (which includes nanomaterials synthesis and sonoluminescence), the mechanochemistry of inorganic solids (including shock wave energy dissipation by metal–organic framework solids), and chemical sensing (specifically, our optoelectronic nose, i.e., colorimetric sensor arrays for the detection of volatile organic compounds). In addition to his academic research, he has had significant entrepreneurial experience. He was the Lead Consultant for Molecular Biosystems Inc., and part of the team that commercialized the first echo contrast agent for medical sonography, Albunex, which became Optison by GE Healthcare. In addition, he was the Founding Consultant for VivoRx Pharmaceuticals and the Co-Inventor of one of the first FDA-approved nanopharmaceuticals, Abraxane (serum albumin microspheres with a paclitaxel core), which is the predominant current delivery system for taxol chemotherapy for breast cancer. Most recently, he invented, developed, and commercialized the "optoelectronic nose," a simple but highly effective technology for the identification and quantification of gas analytes.

Stephen A. Boppart (F'11) received the B.S. degree in electrical and bioengineering and the M.S. degree in electrical engineering from the University of Illinois at Urbana-Champaign, Champaign, IL, USA, in 1990 and 1991, respectively, the Ph.D. degree in medical and electrical engineering from the Massachusetts Institute of Technology, Cambridge, MA, USA, in 1998, and the M.D. degree from Harvard Medical School, Boston, MA, USA, in 2000.

He was a Research Scientist with the Air Force Laser Laboratory, Brooks Air Force Base, San Antonio, TX, USA, where he was engaged in research on developing national and Air Force laser safety standards. Since 2000, he has been a Faculty Member with the University of Illinois at Urbana-Champaign. He is currently an Abel Bliss Professor of Engineering with the Departments of Electrical and Computer Engineering, Bioengineering, and Medicine, the Head of the Biophotonics Imaging Laboratory, and the Director of the Center for Optical Molecular Imaging at the Beckman Institute for Advanced Science and Technology. He has authored more than 300 invited and contributed publications, and more than 700 invited and contributed presentations. He holds more than 40 patents. His research interests include the development of novel optical imaging technologies for biological and medical applications, with particular emphasis on translating these into clinical applications.

Dr. Boppart is a Fellow of IEEE, AAAS, OSA, SPIE, AIMBE, and BMES. He was named one of the top 100 innovators in the world by the *Technology Review Magazine* for his research in medical technology, and received the IEEE Engineering in Medicine and Biology Society Early Career Achievement Award and the IEEE Technical Achievement Award. He was a recipient of the Paul F. Forman Engineering Excellence Award from the Optical Society of America for dedication and advancement in undergraduate research education, and, the international Hans Sigrist Prize for his work in diagnostic laser medicine.